Anionic redox reactions and structural degradation in a cation-disordered rock-salt Li(1.2)Ti(0.4)Mn(0.4)O(2) cathode material revealed by solid-state NMR and EPR

Fushan Geng, Bei Hu, Chao Li, Chong Zhao, Olivier Lafon, Julien Trebosc, Jean-Paul Amoureux, Ming Shen, Bingwen Hu

View Article Online
DOI: 10.1039/D0TA03358H

Anionic Redox and Structural Degradation in Cation-Disordered Rock-Salt $Li_{1.2}Ti_{0.4}Mn_{0.4}O_2$ Cathode Material Revealed by Solid-State NMR and EPR

Fushan Geng,[a] Bei Hu,[a] Chao Li,[a] Chong Zhao,[a] Olivier Lafon,[b,c] Julien Trébosc,[b,d] Jean-Paul Amoureux,[b,e,f] Ming Shen,[a] and Bingwen Hu[a]*

[a] Shanghai Key Laboratory of Magnetic Resonance, State Key Laboratory of Precision Spectroscopy, School of Physics and Electronic Science, East China Normal University, Shanghai 200062, P.R. China.

[b] Univ. Lille, CNRS, Centrale Lille, Univ. Artois, UMR 8181, UCCS – Unité de Catalyse et de Chimie du Solide, F-59000 Lille, France.

[c] Institut Universitaire de France, 1 rue Descartes, F-75231 Paris, France.

[d] Univ. Lille, CNRS-2638, Fédération Chevreul, F-59000 Lille, France.

[e] Bruker Biospin, 34 rue de l'industrie, F-67166 Wissembourg, France.

[f] Riken NMR Science and Development Division, Yokohama, 230-0045 Kanagawa, Japan.

Abstract:

The burgeoning Li-rich cation-disordered rock-salt (DRX) materials have great potential to serve as the cathodes for rechargeable lithium ion batteries. They generally possess high capacities thanks to the participations of both cationic and anionic redox. However, most DRX materials are subject to a large irreversible capacity loss during the first cycle and an undesirable voltage hysteresis between charge and discharge. In this work, solid-state NMR spectroscopy is employed to resolve the manifold local environments in $Li_{1.2}Ti_{0.4}Mn_{0.4}O_2$ as a model sample, and electron paramagnetic resonance (EPR) spectroscopy is used to investigate its electronic properties. Very broad resonances are observed in the ^{7}Li and ^{17}O NMR spectra. The paramagnetic and diamagnetic Li environments are distinguished, and the loss of the diamagnetic Li signal is observed after the first cycle. The

degradation mechanism involved with oxygen loss and transition metal migration is discussed. The formation of the $(O_2)^{n-}$ species and electron holes on oxygen at high voltage are suggested by EPR, and the voltage hysteresis is attributed to the difficulty in reducing the stable O–O bonds. These findings may enrich the understandings on DRX materials to better design high-performance DRX cathodes.

Introduction

To meet the demands for advanced batteries in portable devices and electric vehicles, as well as efficient electrical energy-storage technologies for sustainable power sources, lithium-ion batteries (LIBs) have been developed as one of the most promising solutions.[1, 2] However, cathode materials are currently the key bottleneck that limits the energy density and production costs of LIBs.[3, 4] The current commercialized cathode materials are mostly layered rock-salt materials, such as $LiCoO_2$,[5, 6] $LiNi_xCo_yMn_zO_2$ (NCM),[7-9] and $LiNi_{0.8}Co_{0.15}Al_{0.05}O_2$ (NCA).[10, 11] These materials have a good cycling stability due to the facile insertion of Li ions into the layered structure, but their capacities are limited by the redox activity of transition metal (TM) cations.

Taking advantage of oxygen redox, breakthroughs can be easily achieved in cathode capacity.[12, 13] In particular, in the layered rock-salt materials, the oxidation of oxygen at high voltage can be enabled by an excess of Li ions in the TM layers, giving rise to a prevalence of Li-rich layered oxides.[14-16] Two types of oxygen redox mechanisms have been suggested: the formation of localized electron holes on oxygen which usually exist in Mn-based systems,[17] and the formation of peroxo-like anions $(O_2)^{n-}$ (n = 1, 2, 3) in 4*d*/5*d* and d^0/d^{10} metal systems.[18-20] Both mechanisms lie with the O 2*p* non-bonding state, corresponding to the Li–O–Li configuration arising from the excess of Li ions.

View Article Online
DOI: 10.1039/D0TA03358H

Nevertheless, undesirable problems arise in Li-rich layered oxides when oxygen takes part in the charge compensation. One of the major issues is the hysteresis between charge and discharge, which lowers the energy efficiency. Another issue is the voltage decay occurring during prolonged cycling, which decreases the energy density even if the charge capacity is maintained.[21-23] After several years of research, the origins of these two issues have been primarily related to the anionic redox activity and the migration of TM cations (including the formation of spinel-like structures).[24-27] These troubles still remain as an obstacle on the way to practical application.

The emerging Li-rich cation-disordered rock-salt (DRX) materials are another competitive option, because the migration of Li ions is more favorable through a unique percolation channel devoid of TM ions, called a 0-TM channel,[28] Furthermore, their electrochemical properties can be easily adjusted owing to the large diversity of the selectable TM ions. In particular, DRX materials commonly incorporate early transition metals with d^0 electronic configuration, which tolerates structural distortion and hence, increases the disorder.[29] Several d^0 cation-based DRX materials have been explored, such as Mo-,[30, 31] Nb-,[32] and V-based oxides.[33, 34] Nevertheless, a voltage hysteresis is still observed in these materials and their cycle stability is unsatisfactory. Unlike the ordered layered materials which can be hardly fluorinated,[35] fluorine substitution is easily achieved in the local Li-rich environments of DRX.[36-38] Such strategy was proved to limit the oxygen loss,[31, 39] and allows utilizing only reversible TM redox, which alleviate the voltage hysteresis and structural degradation caused by excessive oxygen redox while maintaining the high capacity of Li-rich compounds.[40, 41]

It is fundamental to understand the structural evolution during charge and discharge for better designing the electrode materials. A few works have investigated the redox behaviors and long-range structural variations in these materials using X-ray absorption spectroscopy (XAS) and X-ray/neutron diffraction (XRD/NPD), respectively, combined with DFT calculations.[32, 42-44] However, there is a

View Article Online
DOI: 10.1039/D0TA05358H

large variety of local environments in DRX materials. Common diffraction techniques only provide insights into the average structure and hence, do not allow to access crucial information on the structure of these disordered materials. By processing neutron or synchrotron X-ray scattering data, pair distribution function (PDF) analysis is able to provide the short-range structure information.[45] In addition, solid-state NMR (ssNMR) spectroscopy with fast magic angle spinning (MAS) is qualified to probe the atomic-scale local structures, which lack long-range positional order.[45] Moreover, *in situ*/*ex situ* NMR can allow the quantification of the Li contents in different surroundings,[46] which would be a very useful information in DRX materials. Furthermore, electron paramagnetic resonance (EPR), which gives information on the local environment of unpaired electrons, can improve our understanding of the redox processes.[47-49]

Herein, we demonstrate that NMR spectroscopy is a powerful tool for determining the Li and O local environments in DRX materials. With the assistance of EPR spectroscopy, we have clarified the changes in local atomic-scale structures during charge and discharge as well as the redox mechanisms. Based on this novel information, several strategies are proposed to circumvent the structural degradation during the first cycle and the voltage hysteresis issue.

Results

Material Characterization

^{17}O-labelled $Li_{1.2}Ti_{0.4}Mn_{0.4}O_2$ (LTMO) was prepared via high-energy shaker-milling with ^{17}O-enriched H_2O, followed by annealing under inert atmosphere. The synchrotron XRD (SXRD) pattern (Fig. 1a) verifies the cubic rock-salt structure ($Fm\bar{3}m$) of the as-prepared sample with no observable impurities, and the Rietveld refinement gives a lattice parameter of 4.143 Å. The particle size was observed by transmission electron microscopy (TEM). As shown in Fig. S1, the diameter of the as-prepared material is ~2 μm with good crystallinity, whereas the sample ball-milled with carbon

View Article Online
DOI: 10.1039/D0TA03358H

additive is crushed into irregular particles with ~150 nm in size. Such a ball-milling procedure is necessary for DRX materials to insure good electrochemical performances.

The crystal structure is illustrated in Fig. 1b. Each cation (Li^+, Ti^{4+}, or Mn^{3+}) is directly bonded to six O anions, and vice versa. With regard to the local environments, each cation has 12 nearest-neighbor cations with 90° bond pathway through oxygen and 6 next-nearest ones with 180° bond pathway. The presence of paramagnetic Mn^{3+} ions near ^7Li or ^{17}O nuclei shifts their NMR signal. This paramagnetic shift stems, in general, from the Fermi contact interaction due to the transfer of unpaired electron spin density from the TM *d* orbitals to the Li/O *s* orbitals through bond pathways. Fig. 1c shows the ^7Li spectrum of the pristine material, corresponding to the isotropic projection of magic angle turning phase-adjusted spinning sidebands 2D spectrum (pjMATPASS).[50] The MATPASS sequence separates in two distinct dimensions, the isotropic and anisotropic shifts, in order to improve the spectral resolution. Along the isotropic projection, the position of the peak is purely determined by the isotropic shift. The isotropic projection of LTMO can be simulated as the sum of two components: a broad line centered at 241 ppm spanning over 1000 ppm and a narrow peak resonating at 0.6 ppm. The broad line, denoted P-Li, is assigned to ^7Li nuclei close to paramagnetic Mn^{3+} ions, which produces Fermi contact shift, whereas the narrow peak, denoted D-Li, is ascribed to ^7Li nuclei with only diamagnetic Li^+ and Ti^{4+} as neighbor cations. Note that the simulation of P-Li peaks as a single Gaussian-Lorentzian line is an approximation, since there are 90 different possible paramagnetic environments for ^7Li nuclei in LTMO (see Supporting Information).

As pjMATPASS experiment is generally assumed to be quantitative,[50] the integrated intensities of deconvoluted signals in Fig. 1c indicates that the fraction of P-Li and D-Li environments in LTMO are 78.2 and 21.8 %, respectively. However, owing to the short relaxation times for the paramagnetic environments, it should be noted that the pjMATPASS experiment could lead to the underestimate of

View Article Online
DOI: 10.1039/D0TA03358H

the P-Li content; and the Li_2O/Li_2CO_3 formed in the bulk or at the surface during the synthesis may lead to the overestimate of the diamagnetic Li environment.

The D-Li signal was also acquired by filtering out the rapidly decaying P-Li signal (Fig. S2). This signal can be simulated as the sum of three components assigned to ^{7}Li environments rich in Li atoms (0.6 ppm, 33.1%), with even amounts of Li and Ti atoms (−25 ppm, 28.2%), and rich in Ti atoms (−65 ppm, 38.6%), respectively. Likewise, owing to the difference between the T_2 relaxation times, it should be noted that there may be some errors for the relative intensities of these different D-Li signals. Monte Carlo simulations indicated that ca. 35% of Li in LTMO is percolating.[51] The 0-TM percolation channels necessarily have a strong correlation with the Li-rich environments. It can be speculated that a larger amount of the 0-TM channels results from a larger amount of the Li-rich environments.

Another common element in cathode materials, oxygen, has rarely been studied by NMR spectroscopy due to the extremely low natural abundance (0.037%) of ^{17}O nuclei.[52, 53] To circumvent this issue, LTMO has been enriched in ^{17}O and the acquired ^{17}O spectra at different fields with different MAS frequencies are shown in Fig. 1d. They exhibit a broad signal with an apparent isotropic peak at ca. 550 ppm. No second-order quadrupolar pattern can be observed since the spectrum is dominated by the distribution of chemical shifts given the large distribution of local environments. The ^{17}O shifts mainly depends on the nature of the six nearest-neighbor cations. When none of them is a Mn^{3+} cation, the position of the peak is determined by the isotropic chemical shift.

Here we try to assign the ^{17}O shifts in terms of the O coordination environments. For O–Li_6 configuration, where the O atom is totally ionic, a shift of ca. 35 ppm should be observed, similar to that in lithium oxide.[54] However, there is no clear signature of such ionic O environment at ca. 35 ppm in the spectrum, suggesting that O–Li_6 configuration is not likely to form in this DRX material.

View Article Online
DOI: 10.1039/D0TA03358H

Hence the observed strong diamagnetic ^{7}Li signal mainly results from Li segregation in domains rich in Ti^{4+}, Li^{+} and O^{2-}. When O atoms are bonded to Ti cations, the orbital interactions lead to higher ^{17}O chemical shifts comparable to 400~800 ppm, which has been measured for Li_2TiO_3 layered rock-salt and Ti_xO_y compounds.[55-57] The fairly broad isotropic resonance (or overlapping resonances) at ca. 550 ppm is just located in this range, which could well correspond to ^{17}O nuclei in the O-Li_xTi_y environments. The broadening of these resonances could result from strong dipolar interaction due to the presence of nearby paramagnetic Mn ions that are not in the first two coordination shell.

When ^{17}O nucleus is bonded to Mn ions, the isotropic shift is determined by the Fermi contact interaction which can result in a very large range of paramagnetic shift. The much broader ^{17}O signal spanning over 7000 ppm (range from −2000 to 5000 ppm) would then be assigned to ^{17}O in domains containing paramagnetic Mn ions. Since Fermi contact shifts are additive, the isotropic shift of O depends on the number of Mn^{3+} among the nearest neighbor cations. The decreasing signal intensity from 550 to 3000 ppm in Fig. 1d indicates that the populations of the O–$Mn_x(Li/Ti)_{6-x}$ (x = 0~6) configurations decrease with increasing x.

Electrochemistry and Redox Processes

The galvanostatic charge and discharge were carried out at 45°C for a better kinetic performance. Fig. 2a shows the voltage profile of LTMO cycled between 1.5 and 4.8 V, which delivers charge and discharge capacities of 358 and 251 mAh g^{-1}, respectively, with a low coulombic efficiency of 70.1%. The theoretical $Mn^{3+/4+}$ redox limit of 131.6 mAh g^{-1} is marked as a vertical dashed line. The sloppy voltage charge profile before this limit is related to the oxidation of Mn^{3+} ions, while the oxygen oxidation beyond this limit shows a flatter voltage profile. No voltage plateau can be seen in the discharge curve.

Cyclic voltammetry (CV) was used to discriminate the redox reactions since it is more sensitive

View Article Online
DOI: 10.1039/D0TA03358H

than the differential capacity (dQ/dV) curves. The first two CV scans between 1.5 and 4.8 V are shown in Fig. 2b. In the first anode process, two obvious anodic peaks located at ca. 3.8 and 4.5 V are observed, corresponding to the Mn^{3+} and O^{2-} oxidations, respectively. When the scan voltage turns back, a very broad cathodic peak can be discerned at around 4.2 V, which is ascribed to the reduction of oxygen. A strong Mn^{4+} reduction peak is observed at ca. 3.3 V, suggesting the good reversibility of the Mn redox. Further reduction of oxygen is evidenced by the two tiny cathodic peaks at around 2.0 and 2.3V. At a low voltage close to 1.5 V, the increasing current density indicates that Mn^{3+} begins to be reduced to Mn^{2+}, as substantiated by XAS in a previous work.[58] The features of the second CV scan are roughly the same as the first cycle. However, the Mn^{3+} oxidation peak drifts to ca. 3.4 V, implying the change of the energy level of Mn 3*d* orbital. The O reduction is still separated into two parts, and the part after Mn reduction becomes even more obvious at ca. 2.1 V as one peak. Irreversible oxygen loss is supposed to take place in the first oxidation process, as the oxidation peak of O is less intense in the second cycle than in the first one. As a conclusion, the CV results show a good reversibility of the Mn redox but a large voltage hysteresis due to the complicated O redox.

Ex situ ^{7}Li and ^{17}O NMR

^{7}Li and ^{17}O NMR experiments were employed to analyze the changes in the local environments in LTMO during the first cycle, and the involved redox mechanisms. Fig. 3a shows the ^{7}Li NMR isotropic spectra of LTMO at different states of charge (SOCs), acquired with the pjMATPASS sequence (The pseudo-2D MATPASS spectra are shown in Fig. S3). These spectra exhibit P-Li and D-Li signals like the pristine sample. The P-Li signal is clearly shifted to high frequency upon charging and shifted back upon discharging, but at the end of the discharge, it does not come back to its initial position. Comparable variations are also observed in the ^{17}O NMR spectra (Fig. 3b), which

View Article Online
DOI: 10.1039/D0TA03358H

were acquired at a high field of 18.8 T in order to reduce the second-order quadrupolar interaction and focus on the paramagnetic shifts. The apparent isotropic peak increases during the charge and decreases during the discharge. Another notable phenomenon is that the spinning sidebands in the ^{17}O NMR spectra are visible at low SOC but are broadened at high SOC, suggesting a more heterogeneous local environments and/or an enhanced ^{17}O quadrupolar interaction and/or increased paramagnetic interactions for high voltage charge.

To analyze the modification of Li local environments during charge and discharge, the ex situ ^{7}Li NMR spectra were also deconvoluted as shown in Fig. S4. However, the use of a single Gaussian-Lorentzian line shape to simulate the P-Li signal leads to inaccuracy on the shifts and integral intensities, and hence we principally focus on the variation tendency. Fig. 3c shows the variation of the Li contents in P-Li and D-Li local environments during charge and discharge. These molar fractions were calculated from the integrated intensities of P-Li and D-Li signals divided by the masses of the active materials and transients, normalized to that of pristine. At the beginning of charging, P-Li and D-Li contents decrease simultaneously. From C40 to C150 as the delithiation proceeds, the amount of D-Li drops faster than that of P-Li, which is in good agreement with the faster migration of Li ions along the 0-TM percolation channel.[28] At the latter stage of the charge, D-Li sites are almost exhausted. Thus, P-Li ions continue to be extracted. During discharging, P-Li recovers quickly while a large proportion of D-Li is irreversibly lost, suggesting the degradation of the D-Li environments. Besides, the electrochemical removal/decomposition of the Li_2O/Li_2CO_3 impurities during cycling may also account for some part of the loss of D-Li.

The ^{7}Li shifts are further analyzed in Fig. 3d by plotting two values: the weighted average shifts and the paramagnetic shifts. The average shift was calculated as the average of the shifts of all the isotropic resonances (P-Li and D-Li) weighted by their intensities (see Supporting Information). The

paramagnetic shift is determined by simulating the P-Li signal. These two values corroborate each other to show the variation tendency of local magnetism around Li. As shown in Fig. 3d, both paramagnetic and average ^{7}Li shifts have steep slopes in the two forms before the $Mn^{3+/4+}$ limit, whereas their increase is slower during the oxidation of oxygen. This observation indicates that the magnitude of Fermi contact shifts on ^{7}Li is different for the unpaired electrons of Mn and O. Therefore, the redox center involved at different SOCs can be recognized from the slope of ^{7}Li shift. During the discharge process, the ^{7}Li shifts exhibit low slope corresponding to the multistep oxygen reductions (4.8~3.5 V and 3~1.5 V, except for the Mn^{3+} to Mn^{2+} reduction near 1.5 V) and steep slope corresponding to the Mn^{4+} to Mn^{3+} reduction (3.5~3 V) in agreement with the above CV study.

Fig. 3e shows the evolution of the ^{17}O shifts for the apparent isotropic peaks. A weighted average calculation cannot be applied to the ^{17}O shifts due to the large anisotropy when using a solid-echo sequence for acquisition. However, the apparent isotropic peak represents the most abundant oxygen environments, and hence it is reasonable to evaluate the changes in oxygen local environments from this peak position. During the oxidation of Mn^{3+} to Mn^{4+}, the peak drifts from 552 to 660 ppm, and then it drifts to 787 ppm at the plateau of O oxidation. At the last charge stage from 4.5 to 4.8 V, the peak shifts back to 750 ppm. When discharging to 1.5 V, the peak drifts to 606 ppm. Unlike the ^{7}Li shifts, the slope of ^{17}O shifts does not significantly vary during the charge and the discharge, which may indicate similar Fermi contact interactions for Mn^{4+}–O and $(O–O)^{n-}$ species. However, we notice that an anomaly occurs in both ^{7}Li and ^{17}O shifts at the end of charging, since we observe a decrease of the ^{17}O peak shift and a steep rise in the ^{7}Li weighted average shift. Such anomaly implies a conversion in the local environment, especially in the electronic structure, and hence EPR experiments were performed to better understand the change in the electronic properties during the charge and the discharge.

View Article Online
DOI: 10.1039/D0TA03358H

Electronic Structure

The molar magnetic susceptibility (χ_m) of the pristine sample was measured in order to determine the spin state of Mn^{3+} ions (Fig. S5). The sample exhibits a paramagnetic behavior above 50 K which follows the Curie-Weiss law and an antiferromagnetic state at very low temperature, analogous to the cation-disordered $Li_{1.25}Nb_{0.25}Mn_{0.5}O_2$ sample.[45] A linear fit of the reciprocal magnetic susceptibility (χ_m^{-1}) versus the temperature between 100 and 300 K gives a Weiss temperature of −41.9 K and a Curie constant of 2.46, which corresponds to an effective magnetic moment $\mu_{eff} = 4.44\ \mu_B$. The spin-only magnetic moment for Mn^{3+} is 4.9 μ_B in high-spin state ($t_{2g}^3\ e_g^1$, $S = 2$) and 2.83 μ_B in low-spin state ($t_{2g}^4\ e_g^0$, $S = 1$), suggesting that the Mn^{3+} ions in LTMO are in the high-spin state. The slight deviation between the observation and the expected value may be due to the second-order spin-orbit coupling effects. The EPR spectrum, which lacks any signal, shown in Fig. 4a, confirms the valence +3 of Mn ions, because Mn^{4+} ions ($S = 3/2$) gives a broad signal at $g \approx 2.0$ while Mn^{3+} ions are EPR-silent due to the integer spin.[48]

The perpendicular-mode EPR spectra are presented into three distinct subfigures for clarity, corresponding to the Mn oxidation, O oxidation, and reduction, as shown in Fig. 4a–c, respectively. A prominent broad line resonating at ca. 90 mT ($g \approx 7.5$) is observed for all charged samples and is assigned to the ferromagnetic resonance, resulting from significant exchange interaction between the Mn ions once Mn^{3+} ions has been oxidized. The molar magnetic susceptibility of two samples, from which ca. 1/3 and 2/3 of Li were extracted, respectively, were further investigated to confirm the ferromagnetism in the charged samples (Fig. S6), and the result shows the presence of short-range ferromagnetism due to the local clusters of Mn ions. As seen in Fig. 4a, the ferromagnetic resonance intensity decreases during the oxidation of Mn^{3+} into Mn^{4+}. However, no signal of Mn^{4+} ions ($g \approx 2.0$) can be observed. Two insights into the structure of LTMO can be inferred from these EPR

View Article Online
DOI: 10.1039/D0TA03358H

observations. First, Mn ions are clustered in the material, otherwise the Mn^{4+} ion surrounded by Li ions should lead to the EPR signal at g ≈ 2.0 due to the lack of exchange interaction. Second, the decrease of the ferromagnetic resonance during the charge indicates that the ferromagnetic interaction between Mn^{3+} and Mn^{4+} is stronger than between Mn^{4+} ions.

At the beginning of oxygen oxidation (C230, Fig. 4b), a new weak signal appears at g ≈ 2.0 is assigned to $(O_2)^{n-}$ (n = 1, 2, 3) species.[49, 59] As compared to the previous report on the $(O_2)^{n-}$ species,[49] the $(O_2)^{n-}$ signal in our work is a lot broader, which may be due to the ferromagnetism in the samples (Fig. S9). However, the $(O_2)^{n-}$ signal disappears for C310 as oxidation proceeds. Oxygen loss has been attested in LTMO at the latter charging stage,[58] and thus it is suggested that the labile $(O_2)^{n-}$ species are further oxidized to O_2 that is released, resulting in the loss of $(O_2)^{n-}$ signal. A few $(O_2)^{n-}$ species may still exist, but are unobservable due to their weak intensity. When charging to the high voltage of 4.8 V (C358), a signal analogous to the $(O_2)^{n-}$ species appears with stronger intensity, which should be ascribed to the localized electron holes on the lone-pair states of O whose other 2*p* orbitals are bonded to Mn.[17] Moreover, a broad line shape centered at g ≈ 2.0 is superimposed on the EPR line, which is unambiguously identified as the line shape of Mn^{4+} ions. It is hence deduced that the electron holes on oxygen disrupt the Mn^{4+}–O^{2-}–Mn^{4+} superexchange coupling so that a part of the Mn^{4+} ions regain the EPR line shape. Additional XPS experiments (Fig. S10) exclude the existence of Mn^{2+} ions at the surface of the high-voltage samples which may contribute to the EPR signals at g ≈ 2.0.

The signal of the Mn^{4+} ions and the electron holes on oxygen vanish for D60 (Fig. 4c), indicating the reduction of oxygen and the rebuilding of the Mn^{4+}–O^{2-}–Mn^{4+} superexchange coupling. It can be concluded that the reduction of holes on oxygen is prior to that of Mn^{4+} ions. Subsequently, the reduction of Mn^{4+} to Mn^{3+} is reflected by the change in the ferromagnetic resonance line shape due

View Article Online
DOI: 10.1039/D0TA05358H

to the difference in the magnetic property of Mn^{3+} and Mn^{4+} cations. When discharging to 1.5 V (D251), a new signal centered at $g \approx 2.0$ is detected. It is assigned to the half-integer spin Mn^{2+} ions, in agreement with the CV curve. The ferromagnetic resonance has not disappeared for the fully discharged sample, indicating that the magnetic ordering is altered in LTMO after electrochemical cycling.

Structural Degradation

As evidenced by ^{7}Li NMR (see Fig. 3c), the Li in paramagnetic environment has a good reversibility during the charge-discharge cycle, while half of the Li in diamagnetic environment is lost. What is at the origin of the degradation of the diamagnetic Li environments? Fig. 5a shows four diffuse scattering patterns around the reciprocal lattices for the pristine LTMO, in accordance with the previous observation on short-range order (SRO).[51] The diffuse scattering patterns preserve their shape and intensity for C150 (Fig. 5b), for which Mn^{3+} is oxidized into Mn^{4+}, indicating that the charge compensation on Mn ions does not give rise to structural evolution. On the contrary, when charging to 4.8 V (Fig. 5c), the ring-like reciprocal halo indicates the lattice distortions, which should be associated with the formation of $(O_2)^{n-}$ species and oxygen release at high voltage. For the fully discharged sample (Fig. 5d), several intensity maxima appear in the diffuse scattering patterns, suggesting a higher SRO after the first cycle, which necessarily involve migration of TM cations. Since the SRO pattern after Mn oxidation does not change, we speculate that the TM cation migration takes place during O oxidation to relax the distorted lattices, resulting in a local disorder-to-order transition.

To verify this hypothesis, the C358 sample was investigated again after being stored into the glove box for two months. As shown in Fig. 6, after two months, the cubic rock-salt structure was transformed into the rhombohedral structure, which means that the original disordered cations were

rearranged into ordered layers. The electronic property of this ordered sample was further investigated by EPR and sXAS (Fig. S12), which indicated that the magnetic coupling was stronger in the rhombohedral structure and the holes on oxygen were refilled. A recent study has suggested a coupling between oxygen redox and TM migration in the layered oxides.[60] In addition, we herein infer that the magnetic ordering transition plays a role in the TM migration as well and the electron spins are prone to alignment in the layers for the rhombohedral structure, which is the alternative (111) plane of the cubic structure. However, the precondition for the TM migration is the existence of vacancies. Upon cycling it is hard to form a long-range order because the vacancies are constantly refilled with Li ions. This dynamic process can only produce a short-range order. The structural degradation must originate from the TM migration during O oxidation, which aggravates the SRO and blocks the 0-TM pathway, resulting in a degradation of electrochemical performance.

Discussion

On the basis of the above investigations, we try now to illuminate the first-cycle anionic redox process in the cation-disordered LTMO, and then correlate it to the structural degradation. Unlike the periodic structure in layered materials, the O environments in DRX materials vary between the different oxygen sub-lattices due to the disordered distribution of cations.[61] Thus, the anionic redox process is complicated. Under the assumption that the cations are randomly distributed, several typical O coordination environments are illustrated in Fig. 7a. Note that the unhybridized O 2*p* orbitals (denoted as $|O_{2p}$) stand along the Li–O–Li axis. They have a higher energy level than the hybridized states, and hence the oxygen oxidation preferentially occurs on these $|O_{2p}$ orbitals. As shown in Fig. 7a, the O–Li_6, O–$TMLi_5$ and O–TM_2Li_4 configurations have three, two and one $|O_{2p}$ lone pairs, respectively, whereas the O 2*p* orbitals in O–TM_3Li_3 and O–TM_6 configurations are all hybridized, and hence are hard to be oxidized. On the basis of the ^{17}O NMR result, the O–Li_6

View Article Online
DOI: 10.1039/D0TA03358H

configurations barely exist in the cation-disordered LTMO, which is contrary to the random cation distribution. This is in agreement with a recent work by Ceder and coworkers,[51] which suggested that the cations in DRX materials are not randomly distributed due to the presence of SRO. Therefore, the $|O_{2p}$ states in LTMO can be classified into two types: the $|O_{2p}$ states under Ti surrounding and the $|O_{2p}$ states under Mn surrounding. The energy of the $|O_{2p}$ states under Mn surrounding are the lower than under Ti surrounding, because Mn t_{2g} orbitals may have a weak π-type interaction with the $|O_{2p}$ states. Besides the $|O_{2p}$ states, the energy level of the hybridized O 2*p* states lies at the bottom, predominating the bonding state between O 2*p* and TM 3*d*/4*s*/4*p*.

The proposed band structure evolution for LTMO upon charging is illustrated in Fig. 7b. When charging to 4.25 V, the electrons are removed from the highest occupied orbital of Mn^{3+}, which is the e_g^* orbital, since the Mn^{3+} ions are in high-spin state. With the exhaustion of the e_g^* electrons beyond 4.25 V, the O^{2-} ions having $|O_{2p}$ states under Ti surrounding begins to be oxidized upon charging to 4.5 V. Owing to the less directional bonding with d^0 Ti ions, the unhybridized O 2*p* orbitals are able to rotate to form σ-type O–O bonds when losing electrons,[20] leading to formation of peroxo-like anions $(O_2)^{n-}$ and the energy splitting of the $|O_{2p}$ state. As a result, the energy level of the anti-bonding orbital σ* is higher than the Mn e_g^* orbital, resulting in the hysteresis of O reduction in the discharge process. In addition, oxygen loss is easier to occur in the Li_2TiO_3-rich environments, as argued by Yabuuchi and coworkers.[62] We further suggest that, accompanied with oxygen release, the TM migration occurs above 4.5 V, resulting in a more serious SRO that impedes the Li diffusion. The irreversible loss of the D-Li environments in the ^{7}Li NMR spectra could result from the oxygen release and the TM migration. And in the CV curves, we observed the shift of the Mn oxidation peak, indicating that the TM migration is irreversible, which alters the Mn redox potential. When charging to 4.8 V, the O^{2-} ions having $|O_{2p}$ states under Mn surrounding starts to be oxidized. Because the

View Article Online
DOI: 10.1039/D0TA03358H

partially filled *d* orbitals which have a strong directionality prevent the rotation of O 2*p* orbitals, the oxidation at 4.8 V creates localized holes on $|O_{2p}$ states instead of the O–O bond. The holes on $|O_{2p}$ states are quite unstable and are easy to cause further structural rearrangement.

During discharging, electrons would fill the empty bands from low to high. The holes on $|O_{2p}$ states are first refilled, showing a small voltage hysteresis. The Mn^{4+} ions are reduced next. The Mn e_g^* band has shifted higher due to the TM migration, leading to a lower $Mn^{3+/4+}$ redox potential. The O–O bonds are broken at last due to the high energy of the anti-bonding orbital σ*, giving rise to a large voltage hysteresis. After the first whole cycle, the local structure in LTMO is changed and the Li and O environments do not return to the pristine state.

The poor first-cycle reversibility is one of the main issues in the cation-disordered LTMO. Besides the side reactions, the irreversible oxygen loss and the TM migration could be responsible for it. We noticed that, in similar reports on LTMO,[32,62] the first-cycle reversibility was much better than in our present work. The discrepancy may come from the sample preparation, leading to the difference in the local O environments which have a great influence on the reversibility. Another issue is the hysteresis of the oxygen reduction, which results from the difficulty in reducing the peroxo-like anions stabilized by the d^0 cations.[19] This is an intrinsic shortcoming in all cathodes utilizing anionic redox. Until recently, breakthroughs have been found via superstructure control or by using a O2-type layered structure.[63-65] Unfortunately, these methods cannot be applied to DRX due to its disordered nature, and thus the hysteresis of the anionic redox in DRX is still waiting to be resolved. Given the broad diversity of the selectable TM ions in DRX materials, the use of only reversible TM redox seems to be a possible solution. The cation-disordered $Li_{1.25}Nb_{0.25}V_{0.5}O_2$ shows an ideal symmetric voltage profile with an excellent reversible capacity of 240 mAh g^{-1},[34] and hence it looks worth developing DRX materials based on early transition metals. Fluorine substitution is

View Article Online
DOI: 10.1039/D0TA03358H

also a versatile strategy to stabilize the O and improve the participation of TM redox.[36, 37, 41] In a word, increasing the participation of TM redox is a promising approach for the improvement of the performance of DRX materials in terms of practical applications.

Conclusions

In this work, we have investigated the evolution of local environments and electronic structure during the first cycle for LTMO via NMR and EPR spectroscopies. This study allowed us to gain new insights into the oxygen redox process and the related structural degradations. For the first time, we have been able to measure the evolution of Li content in different surroundings and the distribution of O local environments in LTMO. Li ions are preferentially removed from the Li-rich regions, in accord with the theory of the 0-TM percolation. Because of the manifold local environments in DRX materials, O redox involves the peroxo-like anions $(O_2)^{n-}$ under Ti surrounding and the electron holes on O 2*p* state under Mn surrounding. An undesirable voltage hysteresis occurs during charge and discharge, which results from the difficulty in reducing the peroxo-like anions owing to their stable O–O bonds. The irreversible loss of Li in the diamagnetic environment is observed by ^{7}Li NMR, indicating the structural degradation after the first cycle. The degradation mechanism could be involved with the oxygen loss and the TM migration at high voltage, which result in a local disorder-to-order transition as the aggravation of SRO which further deteriorates the percolating kinetics. Here, we anticipate that utilizing only TM redox can be a promising solution to improve the first-cycle reversibility and counterbalance the voltage hysteresis upon cycling while maintaining the high DRX capacity, by carefully selecting the TM ions or fluorine substitution.

Experimental

Synthesis

View Article Online
DOI: 10.1039/D0TA03358H

^{17}O-labelled $Li_{1.2}Ti_{0.4}Mn_{0.4}O_2$ was synthesized by a mechanochemical process before calcination. Stoichiometric amounts of Li_2O (Aladdin, 99.99%; 7% excess), TiO_2 (anatase, Aladdin, 99%), and Mn_2O_3 (Alfa Aesar, 98%) with the goal of 0.01 mol of $Li_{1.2}Ti_{0.4}Mn_{0.4}O_2$ were shaker-milled in a 45-mL zirconia grinding bowl with two 8-mm-diameter yttria-stabilized zirconia balls for 30 minutes together with 0.5 mL of $H_2{}^{17}O$ (35~40% ^{17}O, Cambridge Isotope), using a SPEX 8000M Mixer/Mill. The obtained mixture was then pelletized and calcined at 900°C with a heating rate of 5°C min^{-1} for 10 h under argon flow, followed by furnace cooling to room temperature. The pellets were manually ground into powders and stored in an argon-filled glove box.

Electrochemistry

The active material was first shaker-milled with Super P carbon for 1 h at a weight ratio of 7.5:1 in order to pulverize the particles and enhance the electronic conductivity. Excess Super P and polyvinylidene difluoride (PVDF) were then added to the milled powder, followed by manual grinding in an agate mortar. N-Methyl-2-pyrrolidone (NMP) was used to form the slurry, which was casted on an Al foil and vacuum-dried at 100°C overnight. The proportion of active material, carbon and binder in the cathode were 75%, 15% and 10%, respectively. 1 M $LiPF_6$ in a mixture of ethylene carbonate (EC), dimethyl carbonate (DMC) and ethyl methyl carbonate (EMC) (1:1:1 V/V/V) with additive (5%) of fluoroethylene carbonate (FEC) was used as electrolyte. CR2032 coin cells were assembled using Celgard 2300 separators and metallic lithium disks as anode. The mass load was around 3.5 mg cm^{-2} based on active materials. Charge/discharge tests were carried out on a Land CT2001A autocycler at 45°C. The coin cells were cycled to various SOCs and then disassembled carefully inside the glove box to obtain the electrodes which were washed with dimethyl carbonate (DMC) to remove the residual electrolyte. Cyclic voltammetry (CV) test was conducted on a CHI 660e electrochemical workstation within the voltage window of 1.5~4.8 V.

View Article Online
DOI: 10.1039/D0TA03358H

Characterization

The powder XRD pattern of the ^{17}O-labelled $Li_{1.2}Ti_{0.4}Mn_{0.4}O_2$ was recorded at the synchrotron beam line BL14B at Shanghai Synchrotron Radiation Facility (SSRF). Rietveld refinement of the synchrotron XRD (SXRD) pattern was executed with the FullProf Suite software.

Morphological features and lattice fringes of the samples were observed using a high-resolution transmission electron microscope (HRTEM, FEI, TECNAI G2 F20). HRTEM Images were analyzed and processed by the Gatan DigitalMicrograph program.

^{7}Li NMR experiments were performed on a 100 MHz Bruker Avance NMR spectrometer operating at a static magnetic field of 2.35 T and equipped with a 2.5 mm triple resonance HXY MAS probe used in double-resonance mode. ^{7}Li NMR spectra were acquired at a MAS frequency of 25 kHz using zirconia rotors. Temperature regulation was carried out by measuring the paramagnetic shift of protons in a mixture of ferrocene and nickelocene.[66] The actual temperature of the samples was 309 K under the test condition. We carried out rotor-synchronized Hahn-echo ($\pi/2$–τ–π–τ–acq) and pjMATPASS experiments with a $\pi/2$ pulse length of 1.8 μs. The recycle delay was 70 ms, which was long enough to reach thermal equilibrium. The ^{7}Li isotropic shifts were externally referenced to the signal of 1 M LiCl aqueous solution at 0 ppm. The ^{7}Li signals were simulated using the DMFIT program.[67] ^{17}O NMR experiments were performed on a 400 MHz Bruker Avance II NMR spectrometer operating at a static magnetic field of 9.4 T and equipped with a 2.5 mm triple-resonance HXY MAS probe and a 800 MHz Bruker Avance Neo NMR spectrometer operating at a static magnetic field of 18.8 T and equipped with a 1.3 mm triple-resonance HXY MAS probe. The 2.5 and 1.3 mm rotors were spun at a MAS frequency of 30 and 60 kHz, respectively. The temperature was calibrated using the same approach as that employed for experiments at 2.35 T. The actual temperature of the samples was 314 and 316 K in the case of 2.5 and 1.3 mm rotors, respectively.

The ^{17}O spectra were acquired using a rotor-synchronized solid-echo sequence ($\pi/2-\tau-\pi/2-\tau-acq$) with a $\pi/2$ pulse length of 1.5 and 1.08 μs for the acquisition at 9.4 and 18.8 T, respectively. The recycle delay was 10 ms. The ^{17}O isotropic shifts were externally referenced to the signal of pure liquid water at 0 ppm.

Magnetic susceptibility measurements were carried out on a Quantum Design Magnetic Properties Measurement System (MPMS) with a Superconducting Quantum Interference Device (SQUID) magnetometer.

Continuous-wave (CW) X-band EPR spectra were recorded on a Bruker EMX plus 10/12 spectrometer equipped with an Oxford ESR910 Liquid Helium cryostat and a dual-mode microwave cavity. The perpendicular-mode EPR spectra were acquired at a microwave frequency of 9.647~9.649 GHz and room temperature or temperature of 1.8 K using a microwave power of 2 mW and a modulation amplitude of 2 G. The parallel-mode EPR spectra were acquired at a microwave frequency of 9.405~9.408 GHz and room temperature or temperature of 1.8 K using a microwave power of 2 mW and a modulation amplitude of 2 G.

Soft X-ray absorption spectroscopy (sXAS) measurements were recorded at the synchrotron beam line BL08UA at SSRF.

Conflicts of interest

There are no conflicts to declare.

Acknowledgements

This work was supported by National Natural Science Foundation of China (Nos. 21872055, 21902049, 21703068, 21874045) and Shanghai Sailing Program (19YF1413000). Chevreul Institute

View Article Online
DOI: 10.1039/D0TA03358H

(FR 2638), Ministère de l'Enseignement Supérieur, de la Recherche et de l'Innovation, Hauts-de-France Region and FEDER are acknowledged for supporting and funding partially this work. Financial support from the IR-RMN-THC Fr3050 CNRS for conducting the research is gratefully acknowledged. We also acknowledge the support from the Steady High Magnetic Field Facilities of High Magnetic Field Laboratory (CAS) for the EPR and MPMS tests, and the support from Shanghai Synchrotron Radiation Facility for the SXRD (BL14B) and sXAS (BL08UA) experiments. We would like to thank Herve Vezin for inspirational discussion on EPR experiments and Bertrand Doumert for assistance in NMR experiments.

References

1 J. B. Goodenough and K. Park, *J. Am. Chem. Soc.*, 2013, **135**, 1167-1176.
2 D. Larcher and J. Tarascon, *Nat. Chem.*, 2015, **7**, 19-29.
3 W. Li, B. Song and A. Manthiram, *Chem. Soc. Rev.*, 2017, **46**, 3006-3059.
4 W. Lee, S. Muhammad, C. Sergey, H. Lee, J. Yoon, Y. M. Kang and W. Yoon, *Angew. Chem. Int. Edit.*, 2019, **59**, 2578-2605.
5 M. Okubo, E. Hosono, J. Kim, M. Enomoto, N. Kojima, T. Kudo, H. Zhou and I. Honma, *J. Am. Chem. Soc.*, 2007, **129**, 7444-7452.
6 Q. Liu, X. Su, D. Lei, Y. Qin, J. Wen, F. Guo, Y. A. Wu, Y. Rong, R. Kou, X. Xiao, F. Aguesse, J. Bareño, Y. Ren, W. Lu and Y. Li, *Nat. Energy*, 2018, **3**, 936-943.
7 J. Zheng, G. Teng, C. Xin, Z. Zhuo, J. Liu, Q. Li, Z. Hu, M. Xu, S. Yan, W. Yang and F. Pan, *J. Phys. Chem. Lett.*, 2017, **8**, 5537-5542.
8 R. Jung, M. Metzger, F. Maglia, C. Stinner and H. A. Gasteiger, *J. Electrochem. Soc.*, 2017, **164**, A1361-A1377.
9 C. Tian, F. Lin and M. M. Doeff, *Accounts Chem. Res.*, 2017, **51**, 89-96.
10 W. Li, X. Liu, H. Celio, P. Smith, A. Dolocan, M. Chi and A. Manthiram, *Adv. Energy Mater.*, 2018, 1703154.
11 H. Zhang, B. M. May, F. Omenya, M. S. Whittingham, J. Cabana and G. Zhou, *Chem. Mater.*, 2019, **31**, 7790-7798.
12 G. Assat and J. Tarascon, *Nat. Energy*, 2018, **3**, 373-386.
13 B. Li and D. Xia, *Adv. Mater.*, 2017, **29**, 1701054.
14 P. Liu, H. Zhang, W. He, T. Xiong, Y. Cheng, Q. Xie, Y. Ma, H. Zheng, L. Wang, Z. Zhu, Y. Peng, L. Mai and D. Peng, *J. Am. Chem. Soc.*, 2019, **141**, 10876-10882.
15 V. Pimenta, M. Sathiya, D. Batuk, A. M. Abakumov, D. Giaume, S. Cassaignon, D. Larcher and J. Tarascon, *Chem. Mater.*, 2017, **29**, 9923-9936.
16 N. Yabuuchi, K. Yoshii, S. Myung, I. Nakai and S. Komaba, *J. Am. Chem. Soc.*, 2011, **133**, 4404-

View Article Online
DOI: 10.1039/D0TA03358H

4419.
17 K. Luo, M. R. Roberts, R. Hao, N. Guerrini, D. M. Pickup, Y. Liu, K. Edström, J. Guo, A. V. Chadwick, L. C. Duda and P. G. Bruce, *Nat. Chem.*, 2016, **8**, 684-691.
18 E. Mccalla, A. M. Abakumov, M. Saubanère, D. Foix and E. J. Berg, *Science*, 2015.
19 Z. N. Taylor, A. J. Perez, J. A. Coca-Clemente, F. Braga, N. E. Drewett, M. J. Pitcher, W. J. Thomas, M. S. Dyer, C. Collins, M. Zanella, T. Johnson, S. Day, C. Tang, V. R. Dhanak, J. B. Claridge, L. J. Hardwick and M. J. Rosseinsky, *J. Am. Chem. Soc.*, 2019, **141**, 7333-7346.
20 D. Seo, J. Lee, A. Urban, R. Malik, S. Kang and G. Ceder, *Nat. Chem.*, 2016, **8**, 692-697.
21 J. R. Croy, K. G. Gallagher, M. Balasubramanian, B. R. Long and M. M. Thackeray, *J. Electrochem. Soc.*, 2014, **161**, A318-A325.
22 F. Dogan, J. R. Croy, M. Balasubramanian, M. D. Slater, H. Iddir, C. S. Johnson, J. T. Vaughey and B. Key, *J. Electrochem. Soc.*, 2015, **162**, A235-A243.
23 G. Assat, S. L. Glazier, C. Delacourt and J. Tarascon, *Nat. Energy*, 2019, **4**, 647-656.
24 M. Sathiya, A. M. Abakumov, D. Foix, G. Rousse, K. Ramesha, M. Saubanère, M. L. Doublet, H. Vezin, C. P. Laisa, A. S. Prakash, D. Gonbeau, G. VanTendeloo and J. Tarascon, *Nat. Mater.*, 2015, **14**, 230-238.
25 N. Li, S. Hwang, M. Sun, Y. Fu, V. S. Battaglia, D. Su and W. Tong, *Adv. Energy Mater.*, 2019, **9**, 1902258.
26 K. Shimoda, M. Oishi, T. Matsunaga, M. Murakami, K. Yamanaka, H. Arai, Y. Ukyo, Y. Uchimoto, T. Ohta, E. Matsubara and Z. Ogumi, *J. Mater. Chem. A*, 2017, **5**, 6695-6707.
27 G. Assat, A. Iadecola, C. Delacourt, R. Dedryvère and J. Tarascon, *Chem. Mater.*, 2017, **29**, 9714-9724.
28 J. Lee, A. Urban, X. Li, D. Su, G. Hautier and G. Ceder, *Science*, 2014, **343**, 519-522.
29 A. Urban, A. Abdellahi, S. Dacek, N. Artrith and G. Ceder, *Phys. Rev. Lett.*, 2017, **119**, 176402.
30 J. Lee, D. Seo, M. Balasubramanian, N. Twu, X. Li and G. Ceder, *Energ. Environ. Sci.*, 2015, **8**, 3255-3265.
31 J. Lee, J. K. Papp, R. J. Clément, S. Sallis, D. Kwon, T. Shi, W. Yang, B. D. McCloskey and G. Ceder, *Nat. Commun.*, 2017, **8**, 1-10.
32 N. Yabuuchi, M. Nakayama, M. Takeuchi, S. Komaba, Y. Hashimoto, T. Mukai, H. Shiiba, K. Sato, Y. Kobayashi, A. Nakao, M. Yonemura, K. Yamanaka, K. Mitsuhara and T. Ohta, *Nat. Commun.*, 2016, **7**, 1-10.
33 M. A. Cambaz, B. P. Vinayan, H. Euchner, S. A. Pervez, H. Geßwein, T. Braun, A. Gross and M. Fichtner, *Acs Appl. Mater. Inter.*, 2019, **11**, 39848-39858.
34 M. Nakajima and N. Yabuuchi, *Chem. Mater.*, 2017, **29**, 6927-6935.
35 L. Croguennec, J. Bains, M. Ménétrier, A. Flambard, E. Bekaert, C. Jordy, P. Biensan and C. Delmas, *J. Electrochem. Soc.*, 2009, **156**, A349-A355.
36 W. D. Richards, S. T. Dacek, D. A. Kitchaev and G. Ceder, *Adv. Energy Mater.*, 2018, **8**, 1701533.
37 Z. Lun, B. Ouyang, D. A. Kitchaev, R. J. Clément, J. K. Papp, M. Balasubramanian, Y. Tian, T. Lei, T. Shi, B. D. McCloskey, J. Lee and G. Ceder, *Adv. Energy Mater.*, 2019, **9**, 1802959.
38 R. J. Clément, D. Kitchaev, J. Lee and G. Ceder, *Chem. Mater.*, 2018, **30**, 6945-6956.
39 R. A. House, L. Jin, U. Maitra, K. Tsuruta, J. W. Somerville, D. P. Förstermann, F. Massel, L. Duda, M. R. Roberts and P. G. Bruce, *Energ. Environ. Sci.*, 2018, **11**, 926-932.
40 D. A. Kitchaev, Z. Lun, W. D. Richards, H. Ji, R. J. Clément, M. Balasubramanian, D. Kwon, K. Dai, J. K. Papp, T. Lei, B. D. McCloskey, W. Yang, J. Lee and G. Ceder, *Energ. Environ. Sci.*, 2018, **11**, 2159-2171.

41 J. Lee, D. A. Kitchaev, D. Kwon, C. Lee, J. K. Papp, Y. Liu, Z. Lun, R. J. Clément, T. Shi, B. D. McCloskey, J. Guo, M. Balasubramanian and G. Ceder, *Nature*, 2018, **556**, 185-190.
42 D. Chen, W. H. Kan and G. Chen, *Adv. Energy Mater.*, 2019, **9**, 1901255.
43 E. Zhao, L. He, B. Wang, X. Li, J. Zhang, Y. Wu, J. Chen, S. Zhang, T. Liang, Y. Chen, X. Yu, H. Li, L. Chen, X. Huang, H. Chen and F. Wang, *Energy Storage Materials*, 2019, **16**, 354-363.
44 N. Yabuuchi, M. Takeuchi, M. Nakayama, H. Shiiba, M. Ogawa, K. Nakayama, T. Ohta, D. Endo, T. Ozaki, T. Inamasu, K. Sato and S. Komaba, *P. Natl. Acad. Sci.*, 2015, **112**, 7650-7655.
45 M. A. Jones, P. J. Reeves, I. D. Seymour, M. J. Cliffe, S. E. Dutton and C. P. Grey, *Chem. Commun.*, 2019, **55**, 9027-9030.
46 X. Li, M. Tang, X. Feng, I. Hung, A. Rose, P. Chien, Z. Gan and Y. Hu, *Chem. Mater.*, 2017, **29**, 8282-8291.
47 C. Li, M. Shen, X. Lou and B. Hu, *J. Phys. Chem. C*, 2018, **122**, 27224-27232.
48 M. Tang, A. Dalzini, X. Li, X. Feng, P. Chien, L. Song and Y. Hu, *J. Phys. Chem. Lett.*, 2017, **8**, 4009-4016.
49 M. Sathiya, J. B. Leriche, E. Salager, D. Gourier, J. M. Tarascon and H. Vezin, *Nat. Commun.*, 2015, **6**, 1-7.
50 I. Hung, L. Zhou, F. Pourpoint, C. P. Grey and Z. Gan, *J. Am. Chem. Soc.*, 2012, **134**, 1898-1901.
51 H. Ji, A. Urban, D. A. Kitchaev, D. Kwon, N. Artrith, C. Ophus, W. Huang, Z. Cai, T. Shi, J. C. Kim, H. Kim and G. Ceder, *Nat. Commun.*, 2019, **10**, 1-9.
52 I. D. Seymour, D. S. Middlemiss, D. M. Halat, N. M. Trease, A. J. Pell and C. P. Grey, *J. Am. Chem. Soc.*, 2016, **138**, 9405-9408.
53 P. J. Reeves, I. D. Seymour, K. J. Griffith and C. P. Grey, *Chem. Mater.*, 2019, **31**, 2814-2821.
54 M. Leskes, A. J. Moore, G. R. Goward and C. P. Grey, *J. Phys. Chem. C*, 2013, **117**, 26929-26939.
55 T. J. Bastow, P. J. Dirken, M. E. Smith and H. J. Whitfield, *J. Phys. Chem.*, 1996, **100**, 18539-18545.
56 T. J. Bastow and S. N. Stuart, *Chem. Phys.*, 1990, **143**, 459-467.
57 Y. Li, X. Wu, N. Jiang, M. Lin, L. Shen, H. Sun, Y. Wang, M. Wang, X. Ke, Z. Yu, F. Gao, L. Dong, X. Guo, W. Hou, W. Ding, X. Gong, C. P. Grey and L. Peng, *Nat. Commun.*, 2017, **8**, 581-586.
58 K. Zhou, S. Zheng, H. Liu, C. Zhang, H. Gao, M. Luo, N. Xu, Y. Xiang, X. Liu, G. Zhong and Y. Yang, *Acs Appl. Mater. Inter.*, 2019, **11**, 45674-45682.
59 C. Li, C. Zhao, B. Hu, W. Tong, M. Shen and B. Hu, *Chem. Mater.*, 2020, **32**, 1054-1063
60 W. E. Gent, K. Lim, Y. Liang, Q. Li, T. Barnes, S. Ahn, K. H. Stone, M. McIntire, J. Hong, J. H. Song, Y. Li, A. Mehta, S. Ermon, T. Tyliszczak, D. Kilcoyne, D. Vine, J. Park, S. Doo, M. F. Toney, W. Yang, D. Prendergast and W. C. Chueh, *Nat. Commun.*, 2017, **8**, 1-12.
61 M. Ben Yahia, J. Vergnet, M. Saubanère and M. Doublet, *Nat. Mater.*, 2019, **18**, 496-502.
62 Y. Kobayashi, M. Sawamura, S. Kondo, M. Harada, Y. Noda, M. Nakayama, S. Kobayakawa, W. Zhao, A. Nakao, A. Yasui, H. B. Rajendra, K. Yamanaka, T. Ohta and N. Yabuuchi, *Mater. Today*, 2020. (in press)
63 B. Song, M. Tang, E. Hu, O. J. Borkiewicz, K. M. Wiaderek, Y. Zhang, N. D. Phillip, X. Liu, Z. Shadike, C. Li, L. Song, Y. Hu, M. Chi, G. M. Veith, X. Yang, J. Liu, J. Nanda, K. Page and A. Huq, *Chem. Mater.*, 2019, **31**, 3756-3765.
64 R. A. House, U. Maitra, M. A. Pérez-Osorio, J. G. Lozano, L. Jin, J. W. Somerville, L. C. Duda, A. Nag, A. Walters, K. Zhou, M. R. Roberts and P. G. Bruce, *Nature*, 2019, **577**, 502-508.

65 D. Eum, B. Kim, S. J. Kim, H. Park, J. Wu, S. Cho, G. Yoon, M. H. Lee, S. Jung, W. Yang, W. M. Seong, K. Ku, O. Tamwattana, S. K. Park, I. Hwang and K. Kang, *Nat. Mater.*, 2020, 1-9.

66 H. Heise, F. H. Köhler and X. Xie, *J. Magn. Reson.*, 2001, **150**, 198-206.

67 D. Massiot, F. Fayon, M. Capron, I. King, S. Le Calvé, B. Alonso, J. Durand, B. Bujoli, Z. Gan and G. Hoatson, *Magn. Reson. Chem.*, 2002, **40**, 70-76.

View Article Online
DOI: 10.1039/D0TA03358H

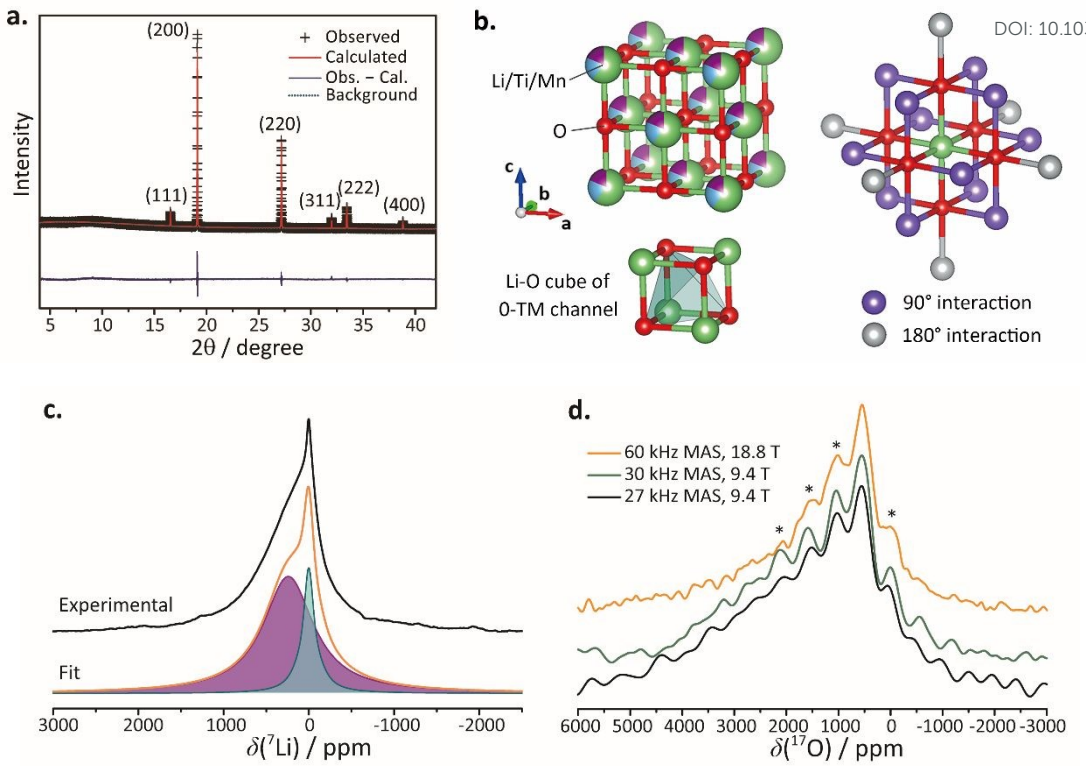

Fig. 1 Crystal structure and local environment of LTMO. a) Synchrotron X-ray diffraction (SXRD, $\lambda = 0.68888$ Å) pattern and Rietveld refinement of the as-synthesized LTMO. b) Crystal structure of LTMO. Left: unit cell of LTMO and the Li–O cube of 0-TM channel. Li diffusion through an intermediate tetrahedral site with no TM ions around has the lowest migration barrier. Right: local environment of Li. Mn ions in the first two nearest neighbors will produce the paramagnetic shifts on ^{7}Li nucleus through 90° or 180° interaction. c) ^{7}Li pjMATPASS NMR spectrum of LTMO at 2.35 T with MAS frequency of 25 kHz. The isotropic resonances can be deconvoluted into P-Li (magenta) and D-Li (cyan) components. d) ^{17}O MAS NMR spectra of LTMO. By varying fields and MAS frequencies, an apparent isotropic peak is assigned at ca. 550 ppm, and spinning sidebands are indicated with asterisks.

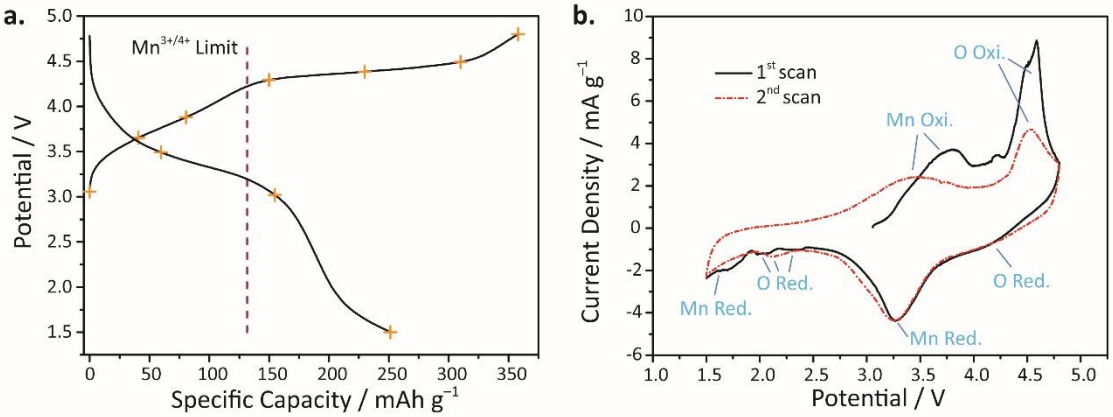

Fig. 2 Electrochemical performance of LTMO half-cell. a) Galvanostatic charge and discharge curve for the first cycle at 10 mA g^{-1} at 45°C. The crosses (+) denote the states of charge (SOCs) for the NMR and EPR characterizations. b) Cyclic voltammogram for the first two scans at a scan rate of 0.02 mV s^{-1}.

View Article Online
DOI: 10.1039/D0TA03358H

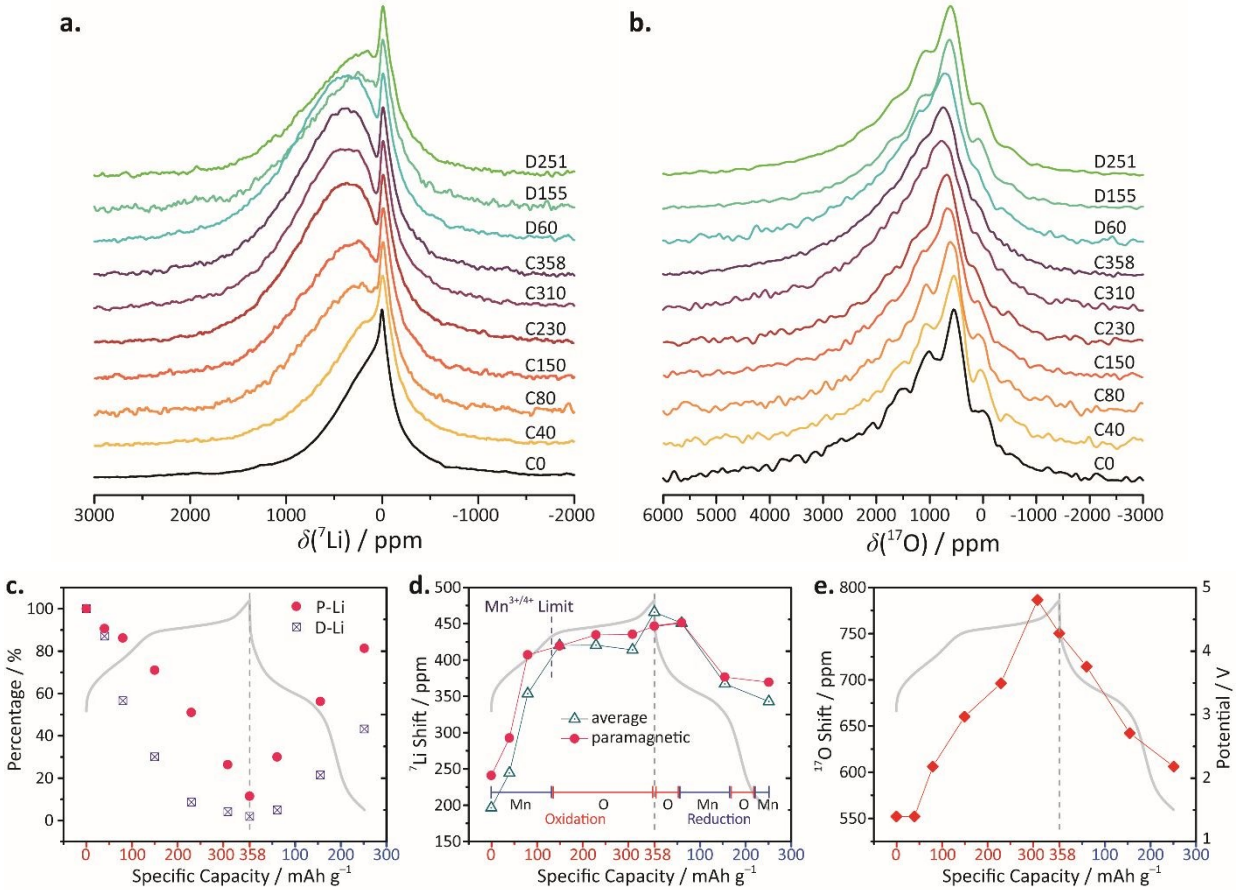

Fig. 3 Ex situ ^{7}Li pjMATPASS (a) and ^{17}O MAS (b) NMR spectra of LTMO at different SOCs. The ^{7}Li and ^{17}O NMR spectra were acquired at a static magnetic field of 2.35 and 18.8 T, respectively. The cycled samples are named as "C/D*X*", where "C" and "D" stands for charge and discharge, respectively, and *X* is the cut-off capacities in mAh g^{-1}. c) Normalized P-Li and D-Li contents in LTMO electrodes at different SOCs. d) Weighted average and paramagnetic ^{7}Li shifts of LTMO at different SOCs. Note that the weighted average shift should never exceed the paramagnetic shift for the same sample, and if not, it is caused by the deviation between the asymmetric spectral line shape and the single Gaussian-Lorentzian line shape in the fitting of paramagnetic shifts. e) Isotropic ^{17}O shifts of LTMO at different SOCs. Galvaniostatic charge and discharge curves are displayed in the background of the subfigures.

View Article Online
DOI: 10.1039/D0TA03358H

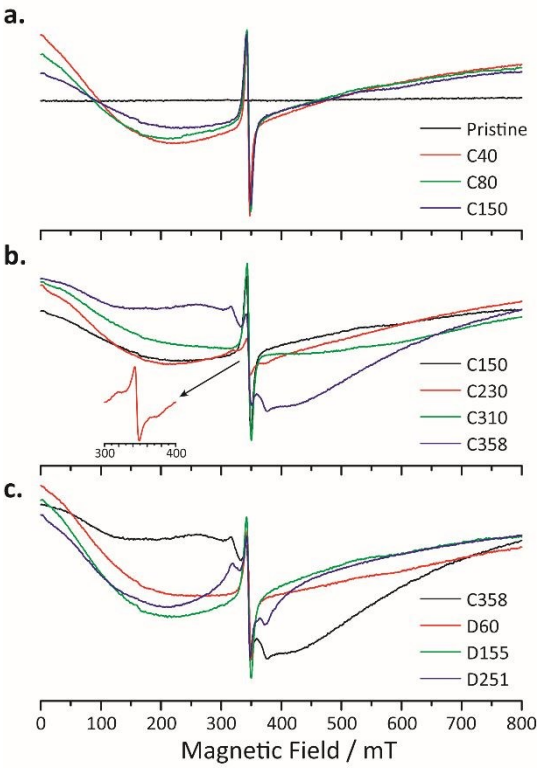

Fig. 4 Ex situ perpendicular-mode CW-EPR spectra of LTMO during the processes of (a) Mn oxidation, (b) O oxidation, and (c) reduction. These EPR measurements were performed at 1.8 K and the results at room temperature are displayed in Fig. S7. The corresponding parallel-mode CW-EPR spectra are displayed in Fig. S8. Signal intensities are normalized based on the mass of each material scraped from the electrodes. The sharp signals centered at ~345 mT (g ≈ 2.0) stem from the delocalized electrons in the conductive carbon black, which can be regarded as an external reference although it may cover up similar signals. The variation on the conductive carbon signals at high voltage is unclear, probably due to the side reaction of carbon oxidation.

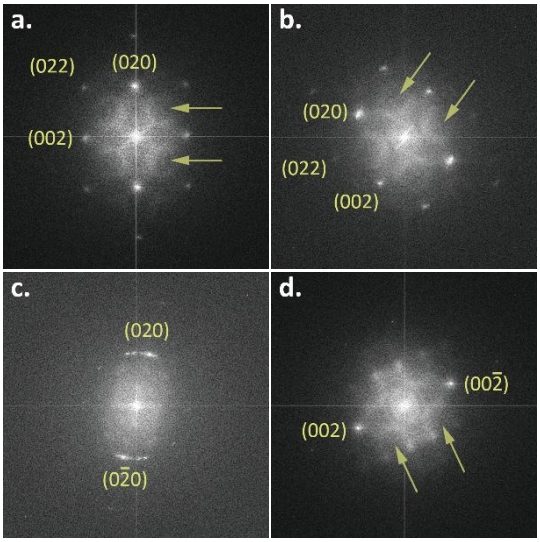

Fig. 5 Fast Fourier transforms (FFT) of the TEM images of: the pristine sample (a), C150 (b), C358 (c), and D251 (d). The direction of observation is along the zone axis [100]. The respective original

TEM images are shown in Fig. S11. The arrows indicate the diffuse scattering patterns around the reciprocal lattices, which are ascribed to the short-range order (SRO).

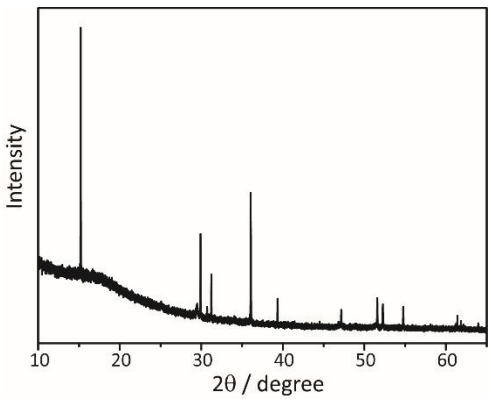

Fig. 6 Synchrotron X-ray diffraction (SXRD, λ = 1.240618 Å) pattern of C358 stored in the glove box for two months. The reflection peaks can be indexed to the rhombohedral structure with R$\bar{3}$m space group.

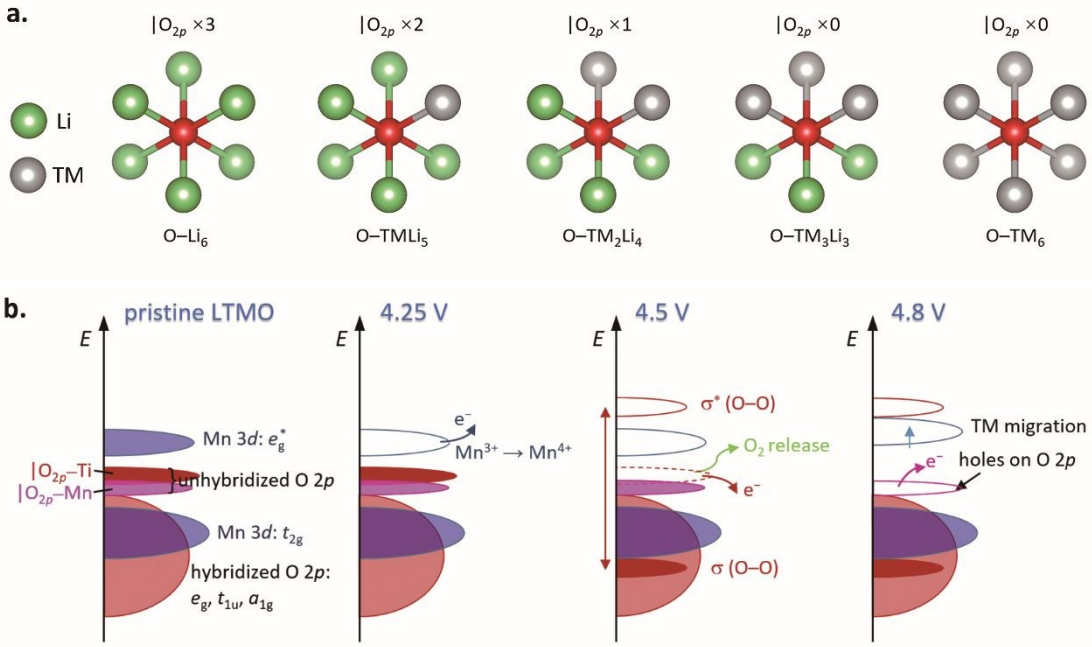

Fig. 7 a) Typical O coordination environments in LTMO. b) Schematic of the proposed band structure evolution for LTMO in the first charge process.

View Article Online
DOI: 10.1039/D0TA03358H

Table of contents entry

The structural evolution of the cation-disordered rock-salt $Li_{1.2}Ti_{0.4}Mn_{0.4}O_2$ is investigated by solid-state NMR and Electron paramagnetic resonance (EPR) spectroscopy during the first cycle. The formation of stable O–O bonds coordinated by Ti ions leads to the voltage hysteresis. The structural degradation is related to the oxygen loss and transition metal migration.